Synthesis of Aluminum-Aluminum Nitride Nanocomposites by Gas-Liquid Reactions I. Thermodynamic and Kinetic Considerations

CECILIA BORGONOVO and MAKHLOUF M. MAKHLOUF

In-situ fabrication of the reinforcing particles directly in the metal matrix is an answer to many of the challenges encountered in manufacturing metal matrix nanocomposite materials. In this method, the nanosized particles are formed directly within the melt by means of a chemical reaction between a specially designed metallic alloy and a reactive gas. The thermodynamic and kinetic characteristics of this chemical reaction dictate the particle size and distribution in the matrix alloy, as well as the nature of the particle/matrix interface, and consequently, they govern many of the material's mechanical and physical properties. This article focuses on aluminum-aluminum-nitride nanocomposite materials that are synthesized by injecting a nitrogen-bearing gas into a molten aluminum alloy. The thermodynamic and kinetic aspects of the process are modeled, and the detrimental role of oxygen is elucidated.

I. INTRODUCTION

ALUMINUM matrix nanoparticle composite materials have mechanical and physical properties that make them attractive for many applications in the aerospace, automotive, and microprocessor industries. These properties derive from the lightweight of aluminum and the attractive properties of aluminum nitride, which include low density (3.026 g cm^{-3}), low average coefficient of thermal expansion [4.5×10^{-6} K (°C)$^{-1}$], and good thermal conductivity [110 to 170 W m^{-1} K(°C)$^{-1}$]. However, producing these materials on a large scale remains difficult despite the many attempts that have been made to overcome the issues associated with their manufacture. Recently, Borgonovo and Makhlouf[1] reviewed the various methods used to manufacture nanocomposite materials and concluded that manufacturing methods that are based on adding *ex-situ* particles to molten metal and employing mechanical stirring to disperse them, as well as methods that are based on liquid infiltration of ceramic substrates, and methods that are based on powder metallurgy have serious limitations when dealing with nanometer size particles. Paramount among these limitations is the high tendency of the particles to cluster and particle/matrix interface debonding. Also the review asserts that more recent fabrication methods, such as spray deposition, ultrasonic-assisted cavitation, and plasma synthesis are not easily scalable and invariably costly. Synthesizing the reinforcing particles inside the metal matrix overcomes many of these issues because the nanoparticles are formed directly within the molten metal by means of a controlled chemical reaction between the liquid alloy and an appropriate gas. *In-situ* particle synthesis ensures good distribution of the reinforcing particles in the matrix alloy, a relatively small particle size, and a clean thermodynamically stable particle/matrix interface.[2] Moreover, production costs of the final component are comparatively low because the expensive nanoparticles are formed in situ. *In-situ* synthesis of nanocomposite materials is typically performed by introducing a reactive gas into a molten metal alloy to cause a chemical reaction that produces the reinforcing particles. The present article focuses on the synthesis of aluminum-aluminum nitride nanocomposites by injecting a nitrogen-bearing gas into molten aluminum that has been prealloyed with magnesium and/or lithium. The underlying thermodynamic and kinetic aspects of the process are investigated, and the mechanism of formation of the aluminum nitride particles is explained. Also, the effect on particle size and particle distribution of the matrix and gas composition, the process temperature and time, and the level of melt stirring during gas injection are elucidated. Finally, the process is mathematically modeled in order to provide means for process control and optimization.

II. APPARATUS AND PROCEDURE FOR SYNTHESIZING AL-ALN NANOCOMPOSITES

Borgonovo and Makhlouf[3] and Borgonovo *et al.*[4] designed and built the apparatus shown schematically in Figure 1 and used it to synthesize Al-AlN nanocomposite material. This apparatus is used here to study the thermodynamic and kinetic aspects of the process. Prior

CECILIA BORGONOVO, Senior Material Scientist at GKN Hoeganaes Corporations, and MAKHLOUF M. MAKHLOUF, Professor, are with the Department of Mechanical Engineering, Worcester Polytechnic Institute, Worcester, MA 01609. Contact e-mail: ceci.borgonovo@gmail.com, mmm@wpi.edu
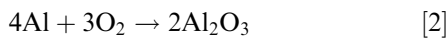
to use, the furnace chamber is thoroughly cleaned in order to remove any contaminants such as dust. A conically shaped alumina crucible is positioned in the furnace with the help of a fiberscope video camera. The camera is inserted from the top of the furnace through a resealable fitting and the cover of the furnace is then closed. Care is taken to locate the crucible in a uniform temperature region in the furnace in order to achieve and maintain the correct temperature for the synthesis reaction. A specially designed gas injection rotating impeller that has been previously coated with boron nitride is inserted from the top into the furnace chamber and its alignment inside the crucible is insured by means of the fiberscope camera. Once the alignment is completed, the camera is extracted and the fittings are placed. A high vacuum pump is then connected to the furnace and the chamber is evacuated to 10^{-2} torr. The furnace is then flushed with high-purity Argon gas. Evacuation and back filling of the chamber with Argon gas is repeated several times in order to remove as much oxygen from the reaction chamber as possible. Then the heating process is started and the temperature is monitored by two k-type thermocouples. During the heating process, a flux of Argon gas is maintained in the furnace. Once the melt has reached the prescribed temperature, the rotating impeller is dipped into the crucible and the reactive gas (either nitrogen or ammonia) is injected into the melt. Two high capacity oxygen getter traps are placed in series along the gas delivery line and the gas is bubbled through them before reaching the furnace. These oxygen removal traps have a removal efficiency that allows less than 1 ppb oxygen in the gas stream.

III. THERMODYNAMIC CONSIDERATIONS

A. The Detrimental Effect of Oxygen

The chemical affinity between oxygen and aluminum is higher than that between nitrogen and aluminum. Consequently, as the Ellingham diagram in Figure 2 shows, aluminum oxidation is more likely to occur than aluminum nitridation. Therefore, it is necessary to determine the minimum amount of oxygen that can be tolerated as impurity in the nitrogen-bearing gas so that nitridation is not hindered.

When oxygen is present in the gas stream, then Eqs. [1] and [2] will occur with Eq. [2] being preferred. Equation [3] can be deduced from Eqs. [1] and [2]:

$$4Al + 2N_2 \rightarrow 4AlN \qquad [1]$$

$$4Al + 3O_2 \rightarrow 2Al_2O_3 \qquad [2]$$

$$2Al_2O_3 + 2N_2 \rightarrow 4AlN + 3O_2. \qquad [3]$$

The Gibbs free energy of formation of Eq. [3], ΔG_{36}, as a function of temperature is given by Eq. [4]:

$$\Delta G_{36} = 4\Delta G_{AlN} + 3\Delta G_{O_2} - 2\Delta G_{Al_2O_3}$$
$$- 2\Delta G_{N_2} = 2078,000 - 185\,T. \qquad [4]$$

The permissible partial pressure of oxygen in the gas stream, P_{O_2}, and hence, the maximum tolerable amount of oxygen for Eq. [3] to proceed toward the right is

$$\Delta G_{36} = -RT\ln P_{36} = -RT\ln \frac{\left(\frac{P_{O_2}}{P_{atm}}\right)^3}{\left(\frac{P_{N_2}}{P_{atm}}\right)^2} \approx -RT\ln\left(\frac{P_{O_2}}{P_{atm}}\right)^3. \qquad [5]$$

Since the nitrogen flow rate is very low (~0.2 L min^{-1}), the calculation can be simplified by assuming that the partial pressure of nitrogen, P_{N_2}, is equal to the total pressure in the reaction system $P_{atm} = 1\,atm = 1.01325 \times 10^5\,Pa$. From Eq. [3] and Eq. [5], and using thermodynamics data from,[5,6] Eq. [6] is derived to describe the change in P_{O_2} with temperature

$$\ln P_{O_2} = 19 - \frac{82,487}{T}. \qquad [6]$$

By employing Eq. [6], it is found that the permissible partial pressure of oxygen for aluminum nitridation at 1273 K (1000 °C) is 5×10^{-20} Pa, which is extremely low, and unlikely to be achieved even with ultrahigh-purity (Grade 5) nitrogen gas. When ammonia gas is employed instead of nitrogen, the partial pressure of oxygen may be determined from Eqs. [7] and [8]:

$$Al_2O_3 + N_2 + 3H_2 \rightarrow 2AlN + 3H_2O \qquad [7]$$

$$H_2 + \frac{1}{2}O_2 \rightarrow H_2O. \qquad [8]$$
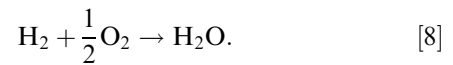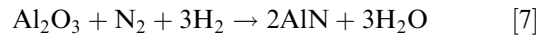
The Gibbs energy of formations for Eqs. [7] and [8], i.e., ΔG_{40} and ΔG_{41}, are

$$\Delta G_{40} = 2\Delta G_{AlN} + 3\Delta G_{H_2O} - \Delta G_{Al_2O_3} - \Delta G_{N_2}$$
$$- 3\Delta G_{H_2} = 313,000 + 29\,T \qquad [9]$$

$$\Delta G_{41} = \Delta G_{H_2O} - \frac{1}{2}\Delta G_{O_2} - \Delta G_{H_2} = -242,000 + 134\,T. \qquad [10]$$

Expressing ΔG_{40} and ΔG_{41} in terms of partial pressures yields Eqs. [11] and [12]:

$$\Delta G_{40} = -RT\ln P_{40} = -RT\ln \frac{\left(\frac{P_{H_2O}}{P_{atm}}\right)^3}{\left(\frac{P_{N_2}}{P_{atm}}\right)\left(\frac{P_{H_2}}{P_{atm}}\right)^3} \qquad [11]$$

$$\approx -RT\ln\left(\frac{P_{H_2O}}{P_{H_2}}\right)^3.$$

$$\Delta G_{41} = -RT\ln P_{41} = -RT\ln \frac{\left(\frac{P_{H_2O}}{P_{atm}}\right)}{\left(\frac{P_{H_2}}{P_{atm}}\right)\left(\frac{P_{O_2\,amm}}{P_{atm}}\right)^{1/2}}. \qquad [12]$$
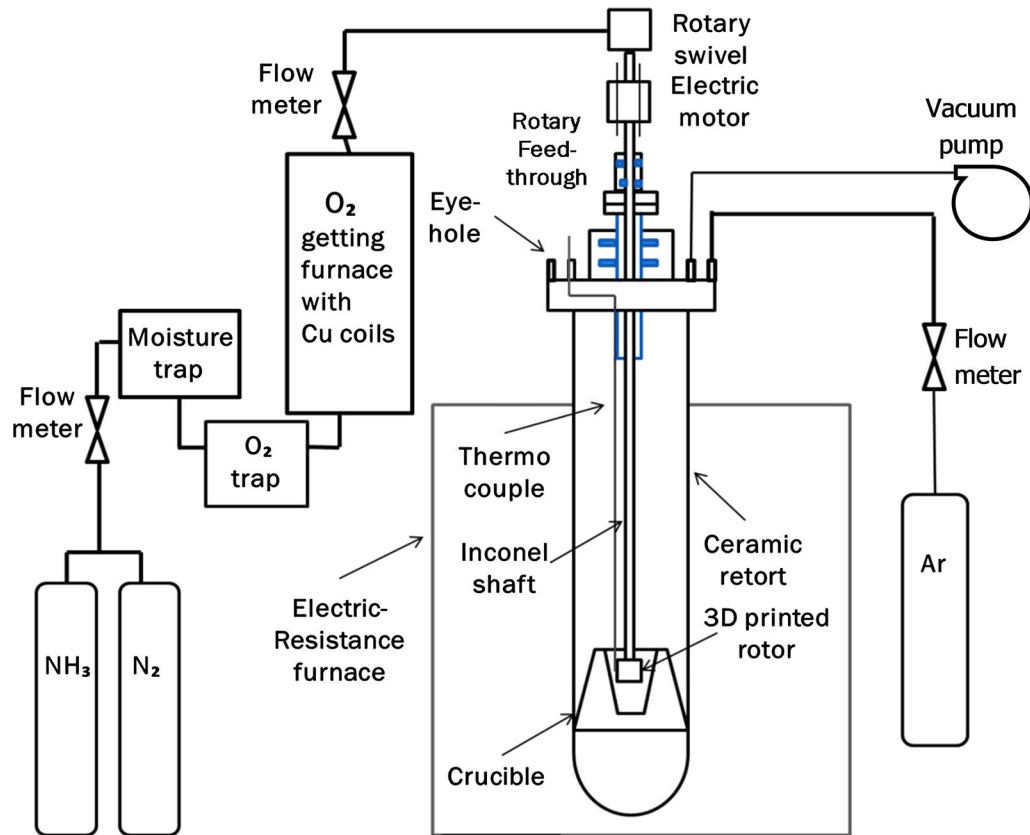
Fig. 1—Schematic representation of the apparatus.

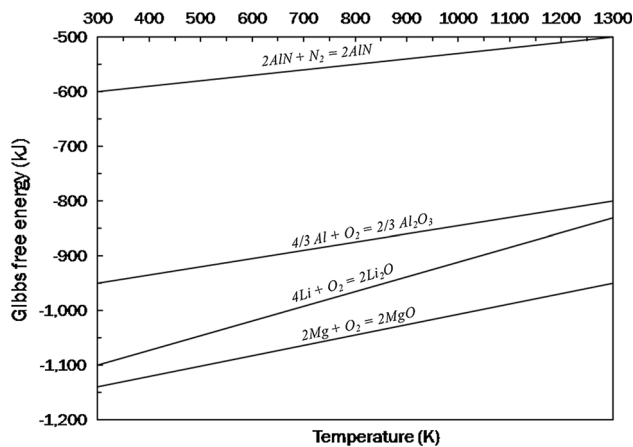

Fig. 2—Ellingham diagram for oxidation and nitridation of Al, Mg, and Li.

The permissible partial pressure of oxygen when ammonia is use for nitridation is determined from Eqs. [9] through [12] to be around 5×10^{-3} Pa, which is possible to achieve even with commercial grade anhydrous ammonia gas. It is reported by Zheng *et al.*[7] that the permissible oxygen partial pressure for nitriding aluminum by nitrogen gas is about 20 orders of magnitude lower than the permissible oxygen partial pressure for nitriding aluminum by ammonia gas (e^{-22} *vs* e^{-2} Pa). It is therefore obvious that nitridation of aluminum is easier when ammonia, rather than nitrogen, is used.

B. *The Role of Alloying Elements, Mg and Li*

Given the harmful effect of oxygen on the nitridation reaction, the oxygen partial pressure in the melt may be lowered by adding elements such as magnesium and/or lithium to aluminum.[3,4,8–10] These elements act as catalysts to 'get' oxygen and mitigate the aluminum oxidation reaction. Magnesium and lithium are ideal for this purpose because the Gibbs free energy for their oxidation is lower than that for oxidation of aluminum, and so oxygen will preferentially combine with them rather than with aluminum. The continuous flow of the nitrogen-bearing gas in the furnace chamber removes the evaporating species (magnesium and MgO, and/or lithium and Li_2O) from the reaction chamber; thus, it maintains a nonequilibrium condition in the melt, which is conducive to high mass flow of the volatilizing lithium (or magnesium). Both magnesium and lithium have been used from Borgonovo and Makhlouf,[3,4] and Borgonovo and Apelian[8,9] to encourage nitridation of aluminum surfaces and also to synthesize AlN powder.

Knowing the partial pressure of oxygen after it reacts with magnesium or lithium allows establishing which one of the two elements is a more effective 'oxygen-getter.' Magnesium volatilizes when Al-Mg alloys are melted at elevated temperature, *i.e.*, 1273 K (1000 °C),

which is typically used to synthesize AlN. The vapor pressure of pure magnesium, P^*_{Mg}, at 1273 K (1000 °C) is 136.45 kPa,[11] and the vapor pressure of magnesium in Al-Mg alloys, P_{Mg}, is given by Eq. [13] in which α_{Mg} is the activity of magnesium in Al-Mg alloys.

$$P_{Mg} = P^*_{Mg}\alpha_{Mg}. \qquad [13]$$

The chemical reaction that leads to formation of MgO is given by Eq. [14], and the Gibbs free energy of this reaction, ΔG_{47}, is given by Eqs. [15] and [16]:

$$Mg + \frac{1}{2}O_2 \rightarrow MgO \qquad [14]$$
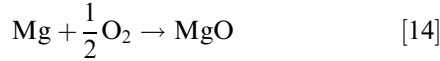
$$\Delta G_{47} = -748,000 + 223\,T \qquad [15]$$

$$\Delta G_{47} = -RT\ln\frac{1}{\left(\frac{P_{Mg}}{P_{atm}}\right)\left(\frac{P_{O_2}}{P_{atm}}\right)^{1/2}}. \qquad [16]$$

Combining Eqs. [13], [15], and [16] yields

$$\ln P_{Mg} = 42.8 - \frac{889,061}{T} - \frac{1}{2}\ln P_{O_2}. \qquad [17]$$

By using these equations, the partial pressure of magnesium and the permissible partial pressure of oxygen in the gas stream when aluminum is alloyed with magnesium are calculated to be 5564 and 3×10^{-28} Pa, respectively.

In the case of alloying aluminum with lithium, phase equilibrium calculations in the Al-Li-O-N system predict that lithium combines with oxygen to form Li_2O at low oxygen levels and $LiAlO_2$ at higher oxygen levels according to Eqs. [18] and [19]:

$$2Li + \frac{1}{2}O_2 \rightarrow Li_2O \qquad [18]$$

$$Li + Al + O_2 \rightarrow LiAlO_2. \qquad [19]$$
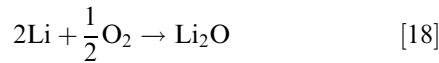
The oxygen content in the high-purity nitrogen-bearing gases typically used in the synthesis of AlN is in the order of parts per billion (ppb), i.e., the partial pressure of oxygen in the nitrogen-bearing gas is $\approx 10^{-9}$ Pa, and Eq. [18] is the relevant reaction. Similar to magnesium, lithium volatilizes at the temperatures used to make AlN. The vapor pressure of pure lithium, P^*_{Li}, at 1273 K (1000 °C) is 136.45 kPa,[12] and the vapor pressure of lithium in Al-Li alloys, P_{Li}, is given by Eq. [20] in which α_{Li} is the activity of lithium in Al-Li alloys[13,14]:

$$P_{Li} = P^*_{Li}\alpha_{Li}. \qquad [20]$$

The chemical reaction that leads to formation of Li_2O is given by Eq. [18] and the Gibbs free energy of this reaction, ΔG_{51}, is given by Eqs. [21] and [22]:

$$\Delta G_{51} = -919,700 + 343\,T \qquad [21]$$

$$\Delta G_{51} = -RT\ln\frac{1}{\left(\frac{P_{Li}}{P_{atm}}\right)^2\left(\frac{P_{O_2}}{P_{atm}}\right)^{1/2}}. \qquad [22]$$

Combining Eqs. [20], [21], and [22] yields

$$\lg P_{Li} = 41.4 - \frac{110,807}{T} - \frac{1}{2}\ln P_{O_2}. \qquad [23]$$

By using these equations, the partial pressure of lithium and the permissible partial pressure of oxygen in the gas stream when aluminum is alloyed with lithium are calculated to be 2635 and 4.7×10^{-49} Pa, respectively. Adding to this, the fact that the energy required to ionize lithium atoms (5.37 v) is lower than that required to ionize magnesium atoms (7.61 v)—which suggests that lithium is more reactive than magnesium—it becomes clear that lithium is much better at removing oxygen from the system than magnesium, and hence, a significantly smaller amount of lithium compared to magnesium is necessary to facilitate aluminum nitridation.

IV. KINETIC CONSIDERATIONS

In order to react with the aluminum melt, nitrogen gas has to diffuse from inside the gas bubble to the bulk liquid aluminum where AlN forms according to the reaction[15]:

$$2Al(l) + N_2(g) = 2AlN(s). \qquad [24]$$

The diffusion-reaction process has been modeled with the two-film approach, which is represented schematically in Figure 3 and is typically used for gas-liquid interactions in bubble column reactors.[16–30] Several assumptions were made in order to facilitate the analysis; they are as follows: (1) the bubble is spherical, (2) diffusion of gas in and out of the bubble, and the consequent bubble shrinkage (or growth) occurs isothermally, (3) the liquid domain is finite and steady, (4) the liquid is incompressible, (5) the gas within the bubble is pure and obeys the ideal gas law, (6) the bubble surface is free of contaminants, (7) liquid-phase resistance controls mass transfer in the melt, (8) Henry's law applies at the gas-liquid interface to couple the gas pressure in the bubble with the dissolved gas concentration at the bubble surface, (9) mass transfer in the liquid phase is ruled by Higbie's penetration theory,[16–30] (10) the initial concentration of nitrogen in the liquid bulk is zero, and finally (11) the confining walls of the crucible have negligible effect on the bubbles.

Close examination of the reaction that leads to the formation of the aluminum nitride particles reveals that the following five steps are involved:
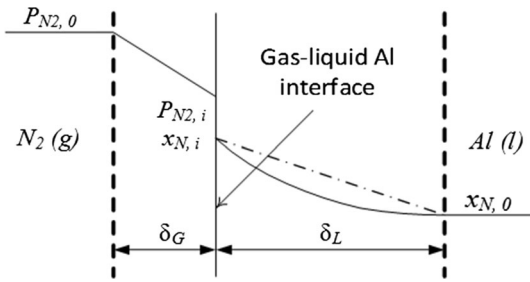
Fig. 3—The 'Two-film' model for N_2 diffusion outside the gas bubble. Reprinted from Ref. [15] with permission from Springer.

Step 1 dissociation of ammonia into hydrogen and nitrogen molecules (this step does not occur when nitrogen is employed as the nitriding gas)

Step 2 mass transfer of nitrogen molecules from the gas bulk to the gas-liquid interface
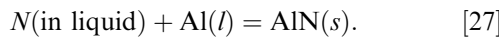
Step 3 chemisorption of nitrogen molecules at the gas-liquid interface according to Eq. [25]

$$N_2(gas) \leftrightarrow N(chemisorbed). \quad [25]$$
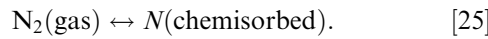
Step 4 mass transfer of nitrogen atoms into the liquid boundary layer according to Eq. [26]

$$N(x_{N,i}) \rightarrow N(x_{N,0}). \quad [26]$$
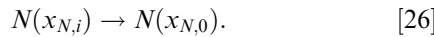
Step 5 growth of solid AlN particles in the liquid boundary layer and in the liquid bulk according to Eq. [27]

$$N(\text{in liquid}) + Al(l) = AlN(s). \quad [27]$$

If nitrogen is used as the nitriding gas, then Step 3, *i.e.*, chemisorption of nitrogen molecules and their conversion into nitrogen atoms at the gas-liquid interface, is rate limiting.[18] This can be concluded from Eq. [28], which gives the rate of chemisorption of nitrogen atoms:

$$r_N = c(2\pi MRT)^{-\frac{1}{2}}\left(P_{N_2,i} - \frac{x_{N,i}}{K_{(12)}}\right)\exp\left(\frac{-E_a}{RT}\right). \quad [28]$$

Equation [28]* shows that once the nitrogen mole-

---

*In Eq. [28], coverage (θ) is accounted for in the constant c.

---

cules are physisorbed by the gas-liquid interface, they have to overcome an energy barrier (E_a) in order to be chemisorbed into the interface. If they do not possess this energy, they eventually become desorbed into the gas bulk. The activation energy E_a for nitrogen chemisorption is very high (308 kJ mol^{-1}) compared to the reversible physisorption state (around 50 kJ mol^{-1}),[15,31] which makes the rate of nitrogen chemisorption very slow. On the other hand,
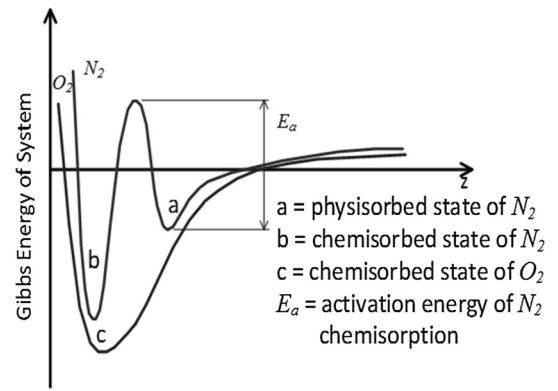

Fig. 4—Change in the energy of the system caused by chemisorption of N_2 and O_2. Reprinted from Ref. [15] with permission from Springer.

chemisorption of oxygen molecules into the gas-liquid interface is much more favorable since it consistently lowers the Gibbs free energy of the system compared to the physisorbed state as shown in Figure 4. Consequently, if present in the nitriding gas, oxygen will occupy the majority of the bonding sites at the gas-liquid interface, thus further hindering the chemisorption of nitrogen into the gas-liquid interface. The extent of occupancy of the available adsorption sites in the gas-liquid interface is given by the 'coverage,' θ, which is expressed as the ratio of occupied adsorption sites q_{ads} and total (saturation) adsorption sites q_{sat}, and the rate of chemisorption is proportional to the number of free adsorption sites; so that[32,33]

$$\theta = \frac{q_{ads}}{q_{sat}} \quad [29]$$

$$r_N \alpha (1 - \theta). \quad [30]$$

Because the rate of chemisorption of nitrogen atoms into the gas-liquid interface is proportional to the number of free adsorption sites, it is important to minimize the amount of oxygen in the nitrogen gas before its injection into the melt.

Another factor that can lower the rate of chemisorption of nitrogen molecules into the gas-liquid interface is the distribution of nitrogen molecules on the interface. If the nitrogen molecules in the gas bulk are unevenly distributed or clustered, then their chemisorption will not be homogenous on the gas-liquid interface. When ammonia is employed as reactive gas, molecular hydrogen dissociates at temperatures higher than 773 K (500 °C) according to Eq. [31] and the aluminum nitridation reaction proceeds according to Eq. [32]:

$$2NH_3(g) = N_2(g) + 3H_2(g) \quad [31]$$

$$2Al(l) + 2NH_3(g) = 2AlN(s) + 3H_2(g). \quad [32]$$
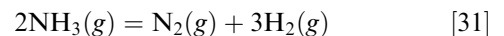
It has been observed[1,3,4] that free hydrogen is an oxygen getter that lowers the oxygen content in the

reaction atmosphere, and by doing so it enhances the adsorption of N_2 molecules at the gas-liquid interface and accelerates the rate of AlN formation. When anhydrous ammonia, rather than pure nitrogen, is employed as the reactive gas, Step 3 becomes faster and the rate-limiting step of the reaction becomes Step 4 because of the very low diffusion coefficient of nitrogen atoms in liquid aluminum. Zheng et al.[7] have analyzed the kinetics of AlN formation in aluminum alloys and found that the mean rate of forming AlN from ammonia is ten times that from nitrogen. The quantity of AlN, W_{AlN}, that forms during a given gas injection time, t, depends on (1) the rate of AlN formation, r_{AlN}, and (2) the total area of the gas bubbles that are dispersed in the melt, A_t, as given by Eq. [33]:

$$W_{AlN} = \int_0^t r_{AlN} A_t dt. \qquad [33]$$

A. Rate of AlN Formation (r_{AlN})

Higbie's penetration theory considers the gas-liquid interface to be composed of a variety of elements continuously brought up to the interface from the bulk of the liquid. The diffusion domain of nitrogen atoms in the liquid is a liquid boundary layer of thickness δ_l given by Eq. [34][16-30]:

$$\delta_l = \frac{\sqrt{D_N \pi t_d}}{2} \text{ where } D_N = 3.75 \times 10^{-7} \exp\left(\frac{-3184}{T}\right). \qquad [34]$$

The local diffusion time, t_d, indicates how long the bubble stays in contact with a single element ahead of its interface, and therefore, it indicates the time available for nitrogen atoms to diffuse into the liquid metal. It depends on the diameter of the bubble, d, and its rising velocity, U_b, according to Eq. [35]:

$$t_d = \frac{d(P_{N_2,I}, x_{N,i})}{U_b(d)}. \qquad [35]$$

The rate of AlN formation r_{AlN} can be written as

$$r_{AlN} = E K_L (x_{N,i} - x_{N,0}). \qquad [36]$$

In Eq. [36], the mass diffusion coefficient of nitrogen in the boundary layer, K_L, is given by Eq. [37] and the enhancement factor, E, which is a nondimensional parameter that accounts for the decreasing level of nitrogen atoms in the melt due to the formation of AlN, is given by Eqs. [38] through [39].[17]:

$$K_L = 2\sqrt{\frac{D_N}{\pi t_d}} \qquad [37]$$

$$E = \frac{\sqrt{M'\left(E_i - \frac{E}{E_i} - 1\right)}}{\tanh\sqrt{M'\left(E_i - \frac{E}{E_i} - 1\right)}} \qquad [38]$$

$$M' = \frac{\pi}{4} K_{AlN} x_{Al} t_d \qquad [39]$$

$$E_i = \sqrt{\frac{D_N}{D_{Al}}} + \frac{x_{N,i}}{x_{Al,i}} \sqrt{\frac{D_{Al}}{D_N}}. \qquad [40]$$

B. Total Area of Gas Bubbles (A_t)

The total surface area of gas bubbles in the melt is determined by the properties of the gas and the liquid, the gas flow rate, and the size of the nozzle, as well as the number of bubbles in the melt, N_b, during the injection time and their residence time in the melt, t_r, as shown in Eq. [41][34]:

$$A_t = N_b A_b = N_b \frac{\pi}{4} d^2 \qquad [41]$$

$$N_b = t_r f_b = \frac{L}{U_b(d)} f_b. \qquad [42]$$

The frequency of formation of gas bubbles, f_b, can be derived from Eqs. [43] through [47] and it is a function of the nozzle diameter of the injection tube, d_{no}, the hydrostatic pressure in the melt at the injection depth, P_{Go}, and of the state of the gas at the inlet of the tube (P_{in}, V_{in}, T_{in}):

$$f_b = \frac{V_g}{V_{bo}} \qquad [43]$$

$$V_{bo} = \frac{4}{3}\pi\left(\frac{d_o}{2}\right)^3 \qquad [44]$$

$$d_o = \left(\frac{6 d_{no} \gamma}{g(\rho_I - \rho_g)}\right)^{1/3} \qquad [45]$$

$$V_g = \frac{P_{in} T}{P_{GO} T_{in}} V_{in} \qquad [46]$$

$$P_{GO} = P_{atm} + \rho_I g L + \frac{4\gamma}{d_{no}} \qquad [47]$$

$$f_b = \frac{g V_{in} P_{in} (\rho_I - \rho_g) T}{\pi \gamma P_{GO} T_{in} d_{no}}. \qquad [48]$$

In terms of gas flow rate, Eq. [48] may be written as

$$f_b = \frac{79.5QT}{0.001(P_{atm} + \rho_l gL) + 4\gamma}. \qquad [49]$$

Previous work[35] calculated A_t and r_{AlN} as constants across the entire liquid domain; as a consequence, these calculations show the amount of reinforcement, W_{AlN}, that form near the bottom regions of the crucible to be equal to that formed in the topmost regions. In reality, this is not the case because the nitrogen bubbles tend to lose mass to the liquid and are subjected to decreasing hydrostatic pressure as they rise. The former effect causes the bubbles to shrink, whereas the latter causes them to expand. Therefore, the bubble diameter varies continuously in the liquid and r_{AlN} and A_t vary with it according to their dependencies on bubble diameter given by Eqs. [35], [37], [41], and [42]. The Navier-Stoke simplified expression for the problem of a rising bubble in a liquid wherein the bubble size varies with time is shown as Eq. [50]:

$$\frac{dr}{dt} = \frac{(P_{N_2,i} - P_I)}{4\eta} - \frac{\gamma}{2\eta}. \qquad [50]$$

The pressure and concentration at the bubble surface are coupled through Henry's law, Eq. [51], and conservation of mass at the interface, Eq. [52]:

$$x_{N,i} = \frac{P_{N_2,i}}{He} \qquad [51]$$

$$\frac{d}{dt}\left(\frac{4\pi P_{N_2,i} r^3}{3RT}\right) = 4\pi r^2 D_N \frac{\partial c}{\partial R}\bigg|_{R=r}. \qquad [52]$$

The concentration gradient at the bubble surface, $\frac{\partial c}{\partial R}\big|_{R=r}$, is determined by means of Fick's second law of diffusion, Eq. [53], with the initial condition for pressure inside the gas bubble expressed by Eq. [47]:

$$\frac{\partial c}{\partial t} = D_N \frac{\partial^2 c}{\partial r^2}. \qquad [53]$$

Figures 5(a) and (b) show, respectively, the progressive decrease in the total surface area of gas bubbles, and the progressive decrease in the number of bubbles as the bubbles rise toward the surface of the melt. Figure 6 was obtained from calculations based on the preceding analysis. It is believed that bubble coalescence is responsible for this decrease in the total surface area of the gas bubbles and the associated decrease in their number. This belief has been confirmed by others, e.g., Ref. [36]. When two bubbles that are rising in a liquid coalesce, the process occurs in three steps:[36–39] (1) the two bubbles collide and trap liquid between them, (2) the surface of the bubbles flatten and the liquid film that was initially trapped between them thins as the liquid drains out, and (3) the two bubbles coalesce into one

The second of the three steps is normally rate limiting. The rate of thinning of the liquid film between the two bubbles may be expressed by Eq. [54] in which l is the original liquid film thickness, R_d is the liquid disk between the coalescing bubbles, Φ is a measure of the surface drag or velocity gradient at the surface due to the absorbed layer of gas, and μ is the static viscosity of the liquid, in this case, aluminum.[39]

$$\frac{dl}{dt} = -\frac{32l^3\gamma}{3\Phi R_d^2 \mu d}. \qquad [54]$$

Equation [54] shows that liquids that have high surface energies, such as aluminum [$\gamma = 813$ dyn/cm at 1273 K (1000 °C)], are more prone to bubble coalescence. Bubble coalescence adversely affects the total concentration of the nitrogen gas that diffuses into the liquid boundary layer ahead of the gas-liquid interface**, which in turn adversely affects the

---

**This is a consequence of the drop in the partial pressure of nitrogen inside the bubble, $P_{N_2,i}$, as the bubbles coalesce (Henry's law).

---

rate of formation of AlN particles.

V. SENSITIVITY ANALYSIS

A. Effect of Melt Temperature (T)

Comparison of Figures 5 and 6 shows that when the temperature of the melt is increased from 1273 K to 1573 K (1000 °C to 1300 °C), the gas-liquid interfacial area doubles and the density of gas bubbles increases by about ten times.

B. Effect of Gas Flow Rate (Q)

The model presented herein is based on the assumption that the effect of gas flow rate on the bubble volume at the time of its detachment from the nozzle, V_{bo}, is negligible. However, when the gas flow rate exceeds a threshold value, the gas flow may transfer into the 'constant-frequency' regime in which V_{bo}, and hence d_{no}, correlates with gas flow rate according to Eq. [55][34]:

$$V_{bo} = 1.378\left(\frac{Q^2}{g}\right)^{3/5}. \qquad [55]$$

Comparison of Figures 6 and 7 confirms the occurrence of the constant-frequency regime as it shows that the number of gas bubbles, N_b, does not increase with increasing flow rate, whereas the gas-liquid interfacial area increases significantly. This is due to the effect on the detaching bubble diameter, d_{no}, which influences the size of the bubble during its rise. This 'additional' gas-liquid interfacial area affects diffusion at the gas-liquid interface and leads to a nitrogen concentration in the melt that is almost three times higher compared to its value with the lower gas flow rate. The increase in
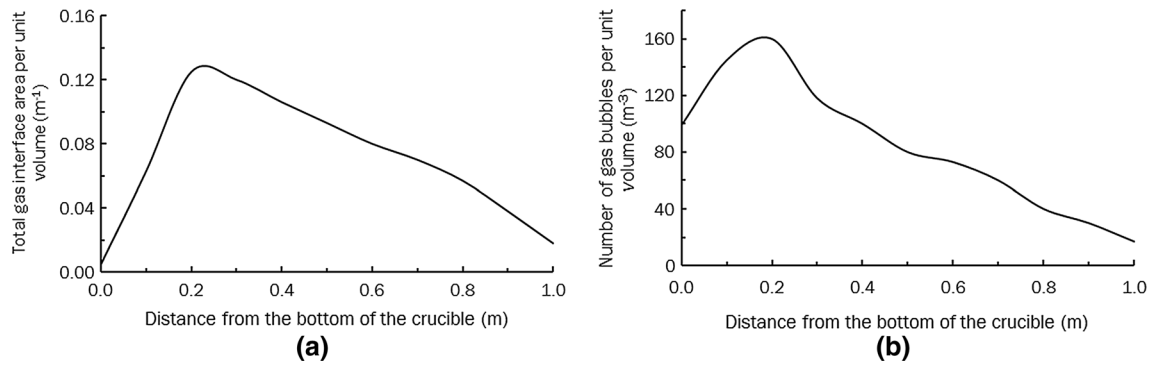
Fig. 5—Calculated (*a*) total gas interface area per unit volume, and (*b*) number of gas bubbles per unit volume both as functions of distance from the bottom of the crucible. $T = 1273$ K (1000 °C), $P_{atm} = 1$ atm, $Q = 0.5$ L/min.
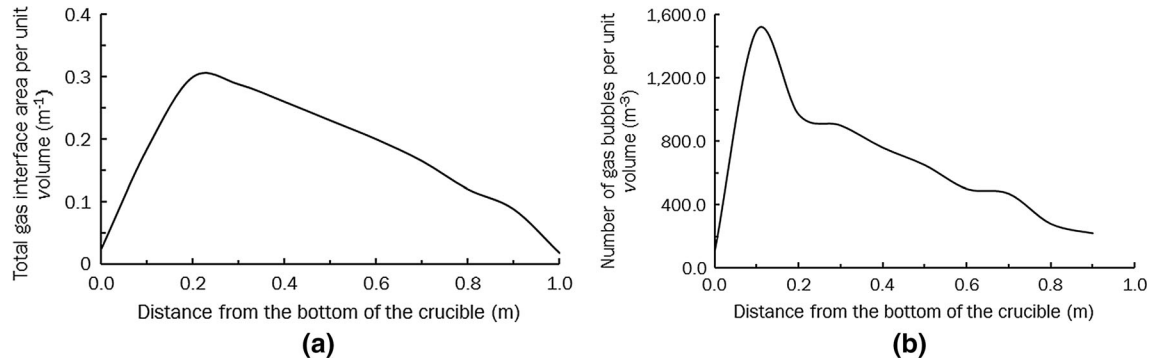

Fig. 6—Calculated (*a*) total gas interface area per unit volume, and (*b*) number of gas bubbles per unit volume both as functions of distance from the bottom of the crucible. $T = 1573$ K (1300 °C), $P_{atm} = 1$ atm, $Q = 0.5$ L/min.
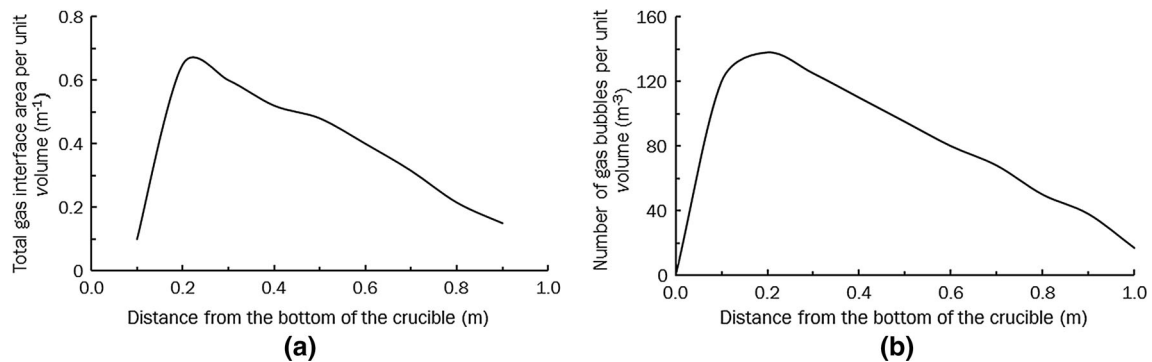

Fig. 7—Calculated (*a*) total gas interface area per unit volume, (*b*) number of gas bubbles per unit volume, and (*c*) concentration of nitrogen per unit volume, all as functions of distance from the bottom of the crucible. $T = 1573$ K (1300 °C), $P_{atm} = 1$ atm, $Q = 1$ L/min.

amount of AlN particles that form with the increase in gas flow rate has been observed by others.[7]

C. *Effect of Pressure in the Reaction Chamber (P$_{atm}$)*

Comparison of Figures 8(b) and 9(b) shows that when the pressure above the melt is increased from 1 to 5 atm, the density number of bubbles, N_b, increases since the frequency of bubble formation, f_b, increases, as suggested by Eq. [48]. The increase in pressure affects the

bubble volume, V_g according to Eq. [46] in that its diameter at the high pressure is smaller than at the low pressure. As a result, the bubble rises more slowly and its residence time in the melt, t_r, is longer, which, according to Eq. [42], further contributes to a higher N_b. Figure 8(a) shows that the total interface area, A_t, reaches a fairly stable value, which is very important to ensure homogeneous distribution of AlN particles in the melt. Figures 9(a) and (b) show that at $P_{atm} = 5$ atm, gas velocity is more or less constant throughout the melt
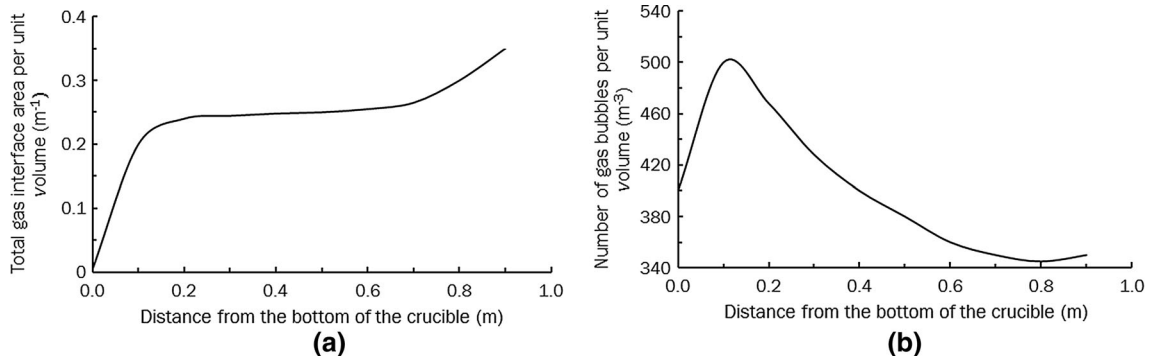
Fig. 8—Calculated (*a*) total gas interface area per unit volume, and (*b*) number of gas bubbles per unit volume, both as functions of distance from the bottom of the crucible. $T = 1573$ K (1300 °C), $P_{atm} = 5$ atm, $Q = 1$ L/min.
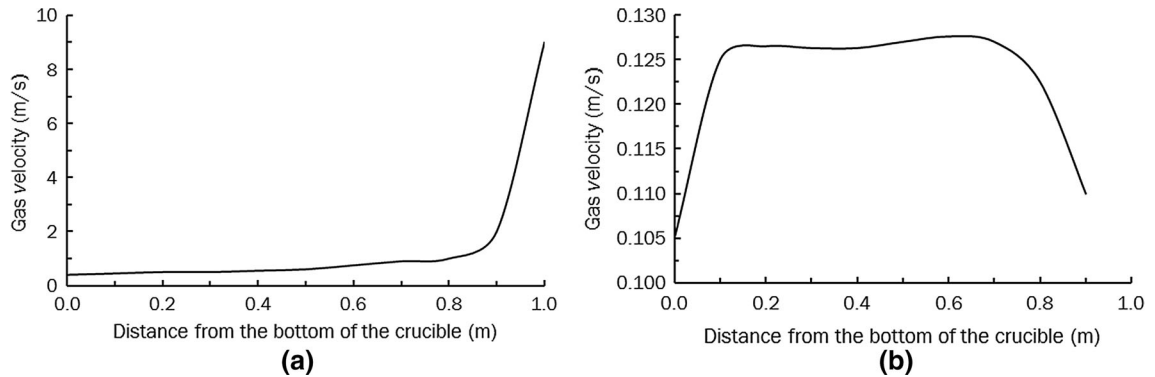

Fig. 9—Calculated gas velocity as a function of distance from the bottom of the crucible (*a*) $P_{atm} = 1$ atm, and (*b*) $P_{atm} = 5$ atm.
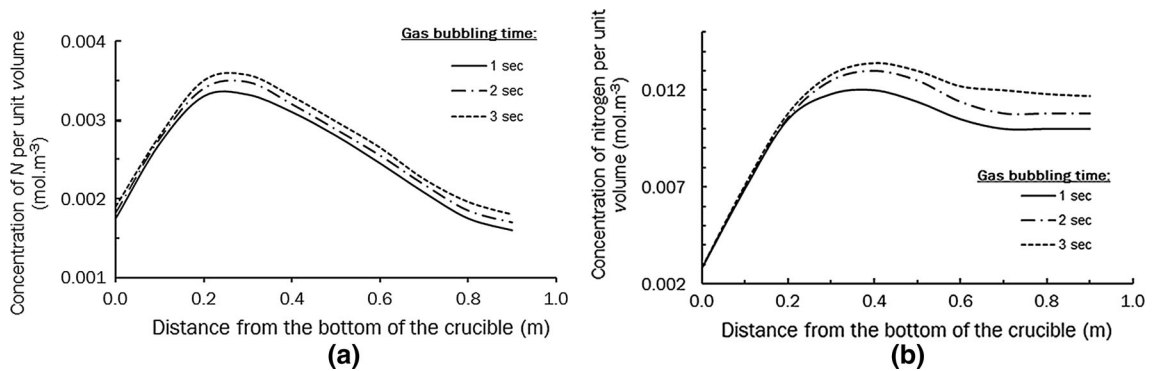

Fig. 10—Calculated concentration of nitrogen per unit volume as a function of distance from the bottom of the crucible. (*a*) $P_{atm} = 1$ atm, and (*b*) $P_{atm} = 5$ atm.

and it is almost 10 times smaller than its value at $P_{atm} = 1$ atm. This results in longer bubble residence times in the melt. The most noteworthy consequence of employing high pressure is the nitrogen concentration profile which, as shown in Figure 10, exhibits values that are three orders of magnitude higher at $P_{atm} = 5$ atm than at $P_{atm} = 1$ atm. Moreover, bubble coalescence is minimized by the increased pressure. It is known that surface tension decreases and liquid viscosity increases with increasing pressure[38,39] also the parameter Φ increases with increased pressure.[35–37] These

changes contribute to reducing the bubble coalescence rate with increased pressure as indicated by Eq. [54]. Furthermore, the frequency of bubble collisions, which is the first step in bubble coalescence, decreases with increasing pressure.

VI. CONCLUSIONS

Synthesizing aluminum-aluminum nitride nanocomposite materials by injecting a nitrogen-bearing gas into

molten aluminum is thermodynamically and kinetically feasible, provided that the oxygen content of the system is maintained at a low level. Thermodynamic and kinetic analysis of the process show that attaining this low oxygen content may be helped by alloying aluminum with magnesium and/or lithium, with lithium being the more efficient of the two elements in this regard. As little as 1 wt pct. lithium is sufficient to suppress oxidation of aluminum and promote its nitridation. The analysis also shows that an increase in process temperature significantly increases the density of reactive gas bubbles. For example, when the process temperature is increased from 1273 K to 1573 K (1000 °C to 1300 °C), the density of reactive gas bubbles increases by about ten times, and the gas-liquid interfacial area doubles. This has positive consequences on the size and distribution of the AlN particles in the matrix alloy. However, high temperature adversely affects the equipment's life expectancy, particularly the rotating impeller and furnace walls. The temperature should be maintained around 1273 K (1000 °C) for best results. In addition, the analysis shows that a relatively high flow rate of the reactive gas increases the gas-liquid interfacial area. The gas-liquid interfacial area affects diffusion at the gas-liquid interface and positively affects the size and distribution of the AlN particles in the matrix alloy. Although high-purity nitrogen and anhydrous ammonia are not prohibitively expensive, for economic reasons, the gas flow rate should be kept no higher than 0.5 L/min. Finally, the analysis shows that an increase in the pressure above the melt increases the density number of reactive gas bubbles and reduces the bubble volume; as a result, the bubbles rise more slowly, their residence time in the melt increases, and their coalescence is minimized.

NOMENCLATURE

α_{Li}	Activation extent of Li in Al-Li alloys at high Li content (>5 pct)
α_{Mg}	Activation extent of Mg in Al-Mg alloys at high Mg content (>5 pct)
γ	Surface tension of aluminum
δ_G	Thickness of the diffusion layer in the gas bulk
δ_L	Thickness of the diffusion layer in the liquid bulk
η	Dynamic viscosity of liquid aluminum
θ	Coverage, defined as $\theta = \frac{q_{ads}}{q_{sat}}$
Φ	Measure of the surface drag or velocity gradient at the surface due to the absorbed layer of the gas
μ	Static viscosity of aluminum
ρ_g	Density of gas
ρ_l	Density of liquid aluminum
A_t	Total gas-liquid interface area
c	Constant in Eq. [28]
d	Bubble diameter
D_{Al}	Diffusion coefficient of aluminum
D_N	Diffusion coefficient of nitrogen in aluminum
d_o	Bubble diameter at bubble detachment

d_{no}	Diameter of the nozzle of the tube
E	Enhancement factor
E_a	Activation energy for chemisorption of nitrogen atoms
f_b	Frequency of formation of gas bubbles
He	Henry's constant for N_2 in liquid Al at $T = 1273$ K (1000 °C)
$K_{(12)}$	Partition coefficient of Reaction 25
K_{AlN}	Equilibrium constant of Eq. [27]
K_L	Mass transfer coefficient of nitrogen in the liquid boundary layer
l	Thickness of liquid film in between coalescing bubbles
L	Depth of the melt
M	Molar mass of the gas molecule
N_b	Number of gas bubbles in the melt
P_{GO}	Pressure of the gas bubble at the moment of detachment from the injection tube
P_l	Pressure in the liquid at the injection level
$P_{N_2,0}$	Partial pressure of nitrogen in the gas bulk
$P_{N_2,i}$	Partial pressure of nitrogen at the gas-liquid interface
P_{in}, T_{in}, V_{in}	Initial state of reactive gas at the inlet of the injection tube
P^*_{Li}	Vapor pressure of pure Li at 1273 K (1000 °C)
P^*_{Mg}	Vapor pressure of pure Mg at 1273 K (1000 °C)
Q	Gas flow rate
q_{ads}	Occupied adsorption sites on the gas-liquid interface
q_{sat}	Total adsorption sites on the gas-liquid interface
R	Bubble radius that varies in the melt. $R = r$ at the interface
R_d	Radius of the liquid disk between the coalescing bubbles
r_N	Rate of chemisorption of nitrogen atoms
T	Temperature
t	Gas injection time
t_d	Local diffusion time
t_r	Residence time of the gas bubble in the melt
U_b	Velocity of the gas bubble
V_{bo}	Volume of gas bubble at bubble detachment
V_g	Volume of the gas bubble
W_{AlN}	Amount of AlN formed
x_{Al}	Concentration of aluminum
$x_{Al,i}$	Concentration of aluminum at the gas-liquid interface
$x_{N,i}$	Concentration of nitrogen atom on the gas-liquid interface
$x_{N,0}$	Concentration of nitrogen atoms in the liquid bulk

REFERENCES

1. C. Borgonovo and M.M. Makhlouf, Transactions of ECCM16—16th European Conference on Composite Materials, Paper no. 23.3.2, Seville, Spain, 2014.
2. R.G. Reddy, US Patent 6,343,640, 2002.

3. C. Borgonovo and M.M. Makhlouf, AFS Transactions, Paper no. 12-067, American Foundry Society, Columbus, OH, 2012.
4. C. Borgonovo, D. Apelian, and M.M. Makhlouf: *JOM*, 2011, vol. 63, pp. 57–64.
5. D.D. Wagman, W.H. Evans, and V.B. Parker, *J. Phys. Chem. Ref. Data,* 1982, vol. 11.
6. L.V. Gurvich, I.V. Veyts, and C.B. Alcock: *Thermodynamic Properties of Individual Substances*, 4th ed., CRC Press, Boca Raton, 1994.
7. Q. Zheng, B. Wu, and R.G. Reddy: *Adv. Eng. Mater.*, 2003, vol. 5, pp. 167–73.
8. C. Borgonovo and D. Apelian: *Mater. Sci. Forum*, 2011, vol. 690, pp. 187–91.
9. C. Borgonovo and D. Apelian: *Mater. Sci. Forum*, 2011, vol. 678, pp. 115–23.
10. C.M. Little, R.A. Murie and M. Warren, US Patent 3,607,046, 1971.
11. M.M. Avedesian and H. Baker: *Magnesium and Magnesium Alloys, ASM Specialty Handbook*, ASM International, Russel Township, 1999.
12. D.W. Jeppson, J.L. Ballif, W.W. Yuan, and B.E. Chou, Hanford Engineering Development Laboratory, Report HEDL-TME 78-15 UC-20, 1978.
13. P.C. Yao and D.J. Fray: *Met. Trans. B*, 1985, vol. 16, pp. 41–46.
14. M.L. Saboungi and M. Blander: *J. Electrochem. Soc.*, 1977, vol. 124, pp. 6–13.
15. Q. Zheng and R.G. Reddy: *J. Mater. Sci.*, 2004, vol. 39, pp. 141–49.
16. S.G. Chatterjee: *Indian Chem. Eng.*, 2009, vol. 51, pp. 177–93.
17. T. Madhavi, A.K. Golder, A.N. Samanta, and S. Ray: *J. Chem. Eng.*, 2007, vol. 128, pp. 95–104.
18. K. Terasaka, J. Oka, and H. Tsuge: *Chem. Eng. Sci.*, 2002, vol. 57, pp. 3757–65.
19. C. Roizard and G. Wild: *Chem. Eng. Sci.*, 2002, vol. 57, pp. 3479–84.
20. R. Krishna and J.M. Baten: *Catal. Today*, 2003, vols. 79–80, pp. 67–75.
21. F. Takemura and Y. Matsumoto: *Chem. Eng. Sci.*, 2000, vol. 55, pp. 3907–17.
22. R.S. Srinivasan, W.A. Gerth, and M.R. Powell: *J. Appl. Physiol.*, 1999, vol. 86, pp. 732–41.
23. S.Q. Yang, B. Du, and L.S. Fan: *Chem. Eng. Sci.*, 2007, vol. 62, pp. 2–27.
24. H. Tsuge, K. Terasaka, W. Koshida, and H. Matsue: *Chem. Eng. Sci.*, 1997, vol. 52, pp. 3415–20.
25. S. Taniguchi, A. Kikuchi, H. Matsuzaki, and N. Bessho: *ISIJ Int.*, 1988, vol. 28, pp. 262–70.
26. J.H. Meldon, O.O. Olawoyin, and D. Bonanno: *Ind. Eng. Chem.*, 2009, vol. 46, pp. 6140–46.
27. A.A.C.M. Beenackers and W.P.M. Swaaij: *Chem. Eng. Sci.*, 1993, vol. 48, pp. 3109–39.
28. M.N.C. Pinheiro: *Int. Commun. Heat Mass*, 2000, vol. 27, pp. 99–108.
29. W. Jang and M.M. Aral: *Environ. Fluid Mech.*, 2003, vol. 3, pp. 173–93.
30. E.P. Elk, M.C. Knaap, and G.F. Versteeg: *Symp. Series IChemE*, 2006, vol. 152, pp. 294–310.
31. P. Atkins and J. De Paula: *Physical Chemistry*, 7th ed., Macmillan, New York, 2002.
32. Lecture on Surface Science and Technology Course: 'Surfaces, Interfaces and their Applications: Adsorbates on Surfaces', Department of Materials, Swiss Federal Institute of Technology, Zurich, Switzerland, 2002.
33. A.T. Hubbard: *Encyclopedia of Surface and Colloid Science*, CRC Press, Boca Raton, 2002.
34. M.A.K. Azad and S.R. Syeda: *J. Chem. Eng.*, 2006, vol. 24, pp. 25–35.
35. W.C. Yang: *Handbook of Fluidization and Fluid-Particle Systems*, CRC Press, Boca Raton, 2003, pp. 772–76.
36. J.J. Carberry: *Chemical and Catalytic Reaction Engineering*, Courier Dover Publications, Mineola, 2001.
37. H.D. Baehr and K. Stephan: *Heat and Mass Transfer*, Springer, New York, 2011.
38. J. Szekely: *Fluid Flow Phenomena in Metals Processing*, Academic Press, New York, 1979.
39. Q. Zheng and R. Reddy: *Metall. Mat. Trans.*, 2003, vol. 34B, pp. 793–804.